

A Complex Quasi-Newton Proximal Method for Image Reconstruction in Compressed Sensing MRI

Tao Hong, Luis Hernandez-Garcia, and Jeffrey A. Fessler

Abstract—Model-based methods are widely used for reconstruction in compressed sensing (CS) magnetic resonance imaging (MRI), using priors to describe the images of interest. The reconstruction process is equivalent to solving a composite optimization problem. Accelerated proximal methods (APMs) are very popular approaches for such problems. This paper proposes a complex quasi-Newton proximal method (CQNPM) for the wavelet and total variation based CS MRI reconstruction. Compared with APMs, CQNPM requires fewer iterations to converge but needs to compute a more challenging proximal mapping called weighted proximal mapping (WPM). To make CQNPM more practical, we propose efficient methods to solve the related WPM. Numerical experiments demonstrate the effectiveness and efficiency of CQNPM.

Index Terms—Compressed sensing, magnetic resonance imaging (MRI), non-Cartesian trajectory, sparsity, wavelets, total variation, second-order.

I. INTRODUCTION

MAGNETIC resonance imaging (MRI) scanners acquire samples of the Fourier transform (known as k-space data) of the image of interest. However, getting an image in MRI is slow since the speed of acquiring k-space data is limited by many constraints, e.g., hardware, physics, and physiology etc., such that improving the acquisition speed is crucial for many MRI applications. Lustig et al. [1] proposed a technique called compressed sensing (CS) MRI that improves the imaging speed significantly. CS MRI allows one to get an image of interest with undersampling data by solving the following composite problem:

$$\mathbf{x}^* = \arg \min_{\mathbf{x} \in \mathbb{C}^N} \underbrace{\frac{1}{2} \|\mathbf{Ax} - \mathbf{y}\|_2^2}_{f(\mathbf{x})} + \lambda h(\mathbf{x}), \quad (1)$$

where $\mathbf{A} \in \mathbb{C}^{ML \times N}$ refers to the forward model describing a mapping from the latent image \mathbf{x} to the acquired k-space data $\mathbf{y} \in \mathbb{C}^{ML}$, $h(\mathbf{x})$ is the regularizer that provides some prior information of \mathbf{x} , $L \geq 1$ denotes the number of coils, and $\lambda > 0$ is a trade-off parameter to balance $f(\mathbf{x})$ and $h(\mathbf{x})$.

Sparsity plays a key role in the success of CS MRI. In general, MR images are not sparse but they can be sparsely represented under some transforms, e.g., total variation (TV) [1], wavelets [2], and transform-learning [3] etc. Recently, more advanced priors or frameworks are introduced for CS

T. Hong and L. Hernandez-Garcia are with the Department of Radiology, University of Michigan, Ann Arbor, MI 48109, USA (Email: {tahong, hernan}@umich.edu).

J. Fessler is with the Department of Electrical and Computer Engineering, University of Michigan, Ann Arbor, MI 48109, USA (Email: fessler@umich.edu).

MRI reconstruction, such as low-rank [4], plug and play [5, 6], model-based deep learning [7], score-based generative models [8], to name a few. This paper focuses on wavelet and TV based CS MRI reconstruction because of their well-established theoretical guarantees and wide clinical use. Here, we are interested in addressing the following minimization problem for image reconstruction in CS MRI:

$$\mathbf{x}^* = \arg \min_{\mathbf{x} \in \mathbb{C}^N} \frac{1}{2} \|\mathbf{Ax} - \mathbf{y}\|_2^2 + \lambda [\alpha \|\mathbf{T}\mathbf{x}\|_1 + (1 - \alpha) \text{TV}(\mathbf{x})], \quad (2)$$

where \mathbf{T} and $\|\cdot\|_1$ denote an abstract wavelet transform and ℓ_1 norm, $\text{TV}(\cdot)$ represents the TV function (see definition in Section II-B), and $\alpha \in [0, 1]$ is used to balance the wavelet and TV terms. For $\alpha = 1$ (respectively, $\alpha = 0$), (2) becomes the wavelet (respectively, TV) based CS MRI reconstruction. Since ℓ_1 and TV functions are nonsmooth, accelerated proximal methods (APMs) [9], which have the optimal convergence rate $O(1/k^2)$ where k is the number of iterations, are very popular algorithms for (2). In [10], Beck et al. proposed a fast iterative shrinkage-thresholding algorithm (FISTA) (a specific type of APM) for wavelet-based image reconstruction and showed a closed-form solution for the related proximal mapping [9]. Beck et al. [11] extended FISTA to solve TV-based image reconstruction and suggested a fast dual gradient descent method to compute the proximal mapping. For more optimization methods and the use of different regularization for the reconstruction in CS MRI, see [12].

Modern MR images are typically acquired using multiple receiver coils and non-Cartesian trajectories, resulting in an expensive forward process from the image to the k-space domains and ill-conditioned or under-determined \mathbf{A} [12]. An ill-conditioned \mathbf{A} can lead to slow reconstruction [13]. To accelerate the recovery process, some preconditioning techniques have been introduced. In [14], Ong et al. proposed a diagonal matrix $\tilde{\mathbf{D}}$ as a preconditioner such that they solve the following problem instead of (1):

$$\mathbf{x}^* = \arg \min_{\mathbf{x} \in \mathbb{C}^N} \frac{1}{2} \|\tilde{\mathbf{D}}^{\frac{1}{2}}(\mathbf{Ax} - \mathbf{y})\|_2^2 + \lambda h(\mathbf{x}). \quad (3)$$

Recently, Iyer et al. [13] developed more effective polynomial preconditioners than $\tilde{\mathbf{D}}$, based on Chebyshev polynomials. Although [13] showed promising results for practical reconstruction, adding such a preconditioner changes the incoherence of \mathbf{A} , which breaks the original theoretical guarantee. For $\alpha \in (0, 1)$, both wavelet and TV are used as regularizers. When we have two nonsmooth terms, the alternating direction method of multipliers (ADMM) [15] is one of the appealing approaches. However, ADMM only provides linear convergence rate $O(1/k)$ [16] and the computation in each iteration

is high because we need to solve a least square problem. In [17–19], the authors proposed several preconditioning methods to solve the least square problem quickly, which reduces the computation time of the whole reconstruction significantly.

Similar to the quasi-Newton methods for smooth minimization problems [20], the authors in [21, 22] developed quasi-Newton proximal methods (QNPMs) for solving composite problems when $\mathbf{x} \in \mathbb{R}^N$. Compared with APMs, QNPMs need fewer iterations to converge which is appealing for problems when computing the gradient $\nabla f(\mathbf{x})$ is expensive. Indeed, the authors in [23–25] applied QNPMs to solving the RED model and the TV based inverse-scattering and X-ray reconstruction and observed faster convergence than APMs. However, QNPMs require computing a weighted proximal mapping (WPM) (defined in (6)) that needs more computation than computing proximal mapping in APMs, so often QNPMs are impractical for many real applications. This paper extends QNPMs to solve (1) when \mathbf{x} is *complex*, which we called complex quasi-Newton proximal methods (CQNPMs). Moreover, we develop efficient methods to compute the WPM and our methods require similar computation as computing proximal mapping in APMs for wavelet and TV based reconstruction. Our numerical experiments on wavelet and TV based CS MRI reconstruction show that CQNPMs converge faster than APMs in terms of the number of iterations and CPU time.

The rest of this paper is organized as follows. Section II first defines some notation and then reviews the formulation of the discretized TV function and the definition of WPM. Section III derives our algorithm. Section IV reports numerical experiments on the wavelet and TV based CS MRI reconstruction. Section V presents some conclusions and future work.

II. PRELIMINARIES

This section first defines some notation that simplifies the following discussion and then describes the discretized TV functions. Finally, we define the WPM that generalizes the well-known proximal mapping.

A. Notation

- Denote by $\mathbf{X} \in \mathbb{C}^{I \times J}$ the matrix form of $\mathbf{x} \in \mathbb{C}^N$ with relation $\mathbf{x} = \text{vec}(\mathbf{X})$ and $\mathbf{X} = \text{mat}(\mathbf{x})$ where $\text{vec}(\cdot)$ denotes a column-stacking operator and $\text{mat}(\cdot)$ is an operator to reshape a vector to its matrix form.
- The (i, j) th (respectively, n th) element of a matrix $\mathbf{X} \in \mathbb{C}^{I \times J}$ (respectively, vector $\mathbf{x} \in \mathbb{C}^N$) is represented as $\mathbf{X}_{i,j}$ (respectively, \mathbf{x}_n).
- \mathcal{P}_1 denotes the set of matrix-pairs (\mathbf{P}, \mathbf{Q}) where $\mathbf{P} \in \mathbb{C}^{(I-1) \times J}$ and $\mathbf{Q} \in \mathbb{C}^{I \times (J-1)}$ satisfy

$$|\mathbf{P}_{i,j}|^2 + |\mathbf{Q}_{i,j}|^2 \leq 1, \quad i = 1, \dots, I-1, \quad j = 1, \dots, J-1,$$

$$|\mathbf{P}_{i,J}| \leq 1, \quad i = 1, \dots, I-1,$$

$$|\mathbf{Q}_{I,j}| \leq 1, \quad J = 1, \dots, J-1.$$

- \mathcal{P}_2 is the set of matrix-pairs (\mathbf{P}, \mathbf{Q}) where $\mathbf{P} \in \mathbb{C}^{(I-1) \times J}$ and $\mathbf{Q} \in \mathbb{C}^{I \times (J-1)}$ satisfy $|\mathbf{P}_{i,j}| \leq 1$, $|\mathbf{Q}_{i,j}| \leq 1, \forall i, j$.
- \mathcal{Z} is the set of vectors $\mathbf{z} \in \mathbb{C}^N$ such that $|\mathbf{z}_n| \leq 1, \forall n$.

- $\mathcal{L} : \mathbb{C}^{(I-1) \times J} \times \mathbb{C}^{I \times (J-1)} \rightarrow \mathbb{C}^{I \times J}$ denotes a linear operator that satisfies

$$\mathcal{L}(\mathbf{P}, \mathbf{Q})_{i,j} = \mathbf{P}_{i,j} + \mathbf{Q}_{i,j} - \mathbf{P}_{i-1,j} - \mathbf{Q}_{i,j-1}, \quad \forall i, j,$$

where we assume that $\mathbf{P}_{0,j} = \mathbf{P}_{I,j} = \mathbf{Q}_{i,0} = \mathbf{Q}_{i,J} = 0, \forall i, j$.

- The adjoint operator of $\mathcal{L} : \mathbb{C}^{I \times J} \rightarrow \mathbb{C}^{(I-1) \times J} \times \mathbb{C}^{I \times (J-1)}$ is

$$\mathcal{L}^T(\mathbf{X}) = (\mathbf{P}, \mathbf{Q}),$$

where $\mathbf{P} \in \mathbb{C}^{(I-1) \times J}$ and $\mathbf{Q} \in \mathbb{C}^{I \times (J-1)}$ are the matrix pairs that satisfy

$$\mathbf{P}_{i,j} = \mathbf{X}_{i,j} - \mathbf{X}_{i+1,j}, \quad i = 1, \dots, I-1, \quad j = 1, \dots, J,$$

$$\mathbf{Q}_{i,j} = \mathbf{X}_{i,j} - \mathbf{X}_{i,j+1}, \quad i = 1, \dots, I, \quad j = 1, \dots, J-1.$$

B. Discretized Total Variation

Assuming zero Neumann boundary conditions for an image $\mathbf{X} \in \mathbb{C}^{I \times J}$, i.e.,

$$\mathbf{X}_{I+1,j} - \mathbf{X}_{I,j} = 0, \quad \forall j \text{ and } \mathbf{X}_{i,J+1} - \mathbf{X}_{i,J} = 0, \quad \forall i,$$

the isotropic and anisotropic TV functions are defined as follows

$$\begin{aligned} \text{TV}_{\text{iso}}(\mathbf{X}) = & \sum_{i=1}^{I-1} \sum_{j=1}^{J-1} \sqrt{(\mathbf{X}_{i,j} - \mathbf{X}_{i+1,j})^2 + (\mathbf{X}_{i,j} - \mathbf{X}_{i,j+1})^2} \\ & + \sum_{i=1}^{I-1} |\mathbf{X}_{i,J} - \mathbf{X}_{i+1,J}| + \sum_{j=1}^{J-1} |\mathbf{X}_{I,j} - \mathbf{X}_{I,j+1}|, \end{aligned} \quad (4)$$

and

$$\begin{aligned} \text{TV}_{\ell_1}(\mathbf{X}) = & \sum_{i=1}^{I-1} \sum_{j=1}^{J-1} \left\{ |\mathbf{X}_{i,j} - \mathbf{X}_{i+1,j}| + |\mathbf{X}_{i,j} - \mathbf{X}_{i,j+1}| \right\} \\ & + \sum_{i=1}^{I-1} |\mathbf{X}_{i,J} - \mathbf{X}_{i+1,J}| + \sum_{j=1}^{J-1} |\mathbf{X}_{I,j} - \mathbf{X}_{I,j+1}|, \end{aligned} \quad (5)$$

respectively. Hereafter, we use $\text{TV}(\mathbf{x})$ to represent either $\text{TV}_{\text{iso}}(\mathbf{X})$ or $\text{TV}_{\ell_1}(\mathbf{X})$.

C. Weighted Proximal Mapping

Given a proper closed convex function $h(\mathbf{x})$ and a Hermitian positive definite matrix $\mathbf{W} : \succ 0 \in \mathbb{C}^{N \times N}$, the WPM associated to h is defined as

$$\text{prox}_h^{\mathbf{W}}(\mathbf{x}) = \arg \min_{\mathbf{u}} \left\{ h(\mathbf{u}) + \frac{1}{2} \|\mathbf{u} - \mathbf{x}\|_{\mathbf{W}}^2 \right\}, \quad (6)$$

where $\|\cdot\|_{\mathbf{W}}$ denotes the \mathbf{W} -norm defined by $\|\mathbf{q}\|_{\mathbf{W}} = \sqrt{\mathbf{q}^H \mathbf{W} \mathbf{q}}$. Here \mathcal{H} denotes Hermitian transpose. Clearly, (6) simplifies to the proximal mapping for $\mathbf{W} = \mathbf{I}_N$ where \mathbf{I}_N represents the identity matrix. Since $h(\mathbf{u}) + \frac{1}{2} \|\mathbf{u} - \mathbf{x}\|_{\mathbf{W}}^2$ is strongly convex, $\text{prox}_h^{\mathbf{W}}(\mathbf{x})$ exists and is unique for $\mathbf{x} \in \text{dom } h$ so that the WPM is well defined.

III. COMPLEX QUASI-NEWTON PROXIMAL METHODS

This section describes a complex quasi-Newton proximal method (CQNPM) for solving (1) with regularizer $h(\mathbf{x}) = \alpha \|\mathbf{Tx}\|_1 + (1 - \alpha) \text{TV}(\mathbf{x})$. That regularizer was originally presented in [1] for CS MRI reconstruction. Here, we consider $\mathbf{T} \in \mathbb{C}^{N \times N}$ as a wavelet transform. Algorithm 1 gives the detailed steps of the proposed CQNPM. Note that Algorithm 1 is identical to the proximal methods [9] for $\mathbf{B}_k = \mathbf{I}_N$. In this paper, we choose \mathbf{B}_k as an approximation of the Hessian of $f(\mathbf{x})$. We select the Symmetric Rank-1 (SR1) method [20] to define \mathbf{B}_k . Algorithm 2 presents the implementation details of SR1.

Algorithm 1 Proposed Complex Quasi-Newton Proximal Method (CQNPM).

Initialization: \mathbf{x}_1 .

Iteration:

- 1: **for** $k = 1, 2, \dots$ **do**
- 2: pick the step-size a_k and the weighting \mathbf{B}_k .
- 3: $\mathbf{x}_{k+1} \leftarrow \text{prox}_{a_k \lambda h}^{\mathbf{B}_k} (\mathbf{x}_k - a_k \mathbf{B}_k^{-1} \nabla_{\mathbf{x}} f(\mathbf{x}_k))$.
- 4: **end for**

Algorithm 2 SR1 updating.

Initialization: $\gamma > 1$, $\delta = 10^{-8}$, $\Xi > 0$ a fixed real scalar, \mathbf{x}_k , \mathbf{x}_{k-1} , $\nabla f(\mathbf{x}_k)$, and $\nabla f(\mathbf{x}_{k-1})$.

- 1: **if** $k = 1$ **then**
- 2: $\mathbf{B}_k \leftarrow \Xi \mathbf{I}$.
- 3: **else**
- 4: Set $\mathbf{s}_k \leftarrow \mathbf{x}_k - \mathbf{x}_{k-1}$ and $\mathbf{m}_k \leftarrow \nabla f(\mathbf{x}_k) - \nabla f(\mathbf{x}_{k-1})$.
- 5: Compute $\tau_k \leftarrow \gamma \frac{\|\mathbf{m}_k\|_2^2}{\langle \mathbf{s}_k, \mathbf{m}_k \rangle}$. % $\langle \mathbf{a}, \mathbf{b} \rangle = \mathbf{b}^H \mathbf{a}$
- 6: **if** $\tau < 0$ **then**
- 7: $\mathbf{B}_k \leftarrow \Xi \mathbf{I}$.
- 8: **else**
- 9: $\mathbf{H}_0 \leftarrow \tau_k \mathbf{I}$.
- 10: $\mathbf{u}_k \leftarrow \mathbf{m}_k - \mathbf{H}_0 \mathbf{s}_k$.
- 11: **if** $|\langle \mathbf{u}_k, \mathbf{s}_k \rangle| \leq \delta \|\mathbf{s}_k\|_2 \|\mathbf{u}_k\|_2$ **then**
- 12: $\mathbf{u}_k \leftarrow \mathbf{0}$.
- 13: **end if**
- 14: $\mathbf{B}_k \leftarrow \mathbf{H}_0 + \frac{\mathbf{u}_k \mathbf{u}_k^H}{\langle \mathbf{m}_k - \mathbf{H}_0 \mathbf{s}_k, \mathbf{s}_k \rangle}$.
- 15: **end if**
- 16: **end if**
- 17: **Return:** \mathbf{B}_k

The dominant computation in Algorithm 1 is computing the WPM at Step 3 which could be as hard as solving (1) for a general \mathbf{B}_k . However, we find one can compute $\text{prox}_{\lambda h}^{\mathbf{B}_k}(\cdot)$ as easily as the case when $\mathbf{B}_k = \mathbf{I}_N$ by using the structure of \mathbf{B}_k . Next we discuss how to obtain the WPM efficiently.

To compute the WPM $\text{prox}_{\lambda h}^{\mathbf{B}_k}(\mathbf{v}_k)$ at k th iteration, we need to solve the following problem

$$\min_{\mathbf{x} \in \mathbb{C}^N} \|\mathbf{x} - \mathbf{v}_k\|_{\mathbf{B}_k}^2 + 2\bar{\lambda} [\alpha \|\mathbf{Tx}\|_1 + (1 - \alpha) \text{TV}(\mathbf{x})], \quad (7)$$

where $\mathbf{v}_k = \mathbf{x}_k - a_k \mathbf{B}_k^{-1} \nabla_{\mathbf{x}} f(\mathbf{x}_k)$ and $\bar{\lambda} = a_k \lambda$. A difficulty of (7) is the nonsmoothness of $\|\cdot\|_1$ and $\text{TV}(\cdot)$. To address this difficulty, we consider a dual approach for (7) that is similar

to Chambolle's approach for TV based image reconstruction [26]. Proposition 1 describes the dual problem of (7) and the relation between the primal and dual optimal solutions.

Proposition 1. *Let*

$$(\mathbf{z}^*, \mathbf{P}^*, \mathbf{Q}^*) = \underset{\substack{\mathbf{z} \in \mathcal{Z} \\ (\mathbf{P}, \mathbf{Q}) \in \mathcal{P}}}{\text{argmin}} \|\mathbf{w}_k(\mathbf{z}, \mathbf{P}, \mathbf{Q})\|_{\mathbf{B}_k}^2$$

where $\mathbf{w}_k(\mathbf{z}, \mathbf{P}, \mathbf{Q}) = \mathbf{v}_k - \bar{\lambda} \mathbf{B}_k^{-1} (\alpha \mathbf{T}^H \mathbf{z} + (1 - \alpha) \text{vec}(\mathcal{L}(\mathbf{P}, \mathbf{Q})))$ and $\mathcal{P} = \mathcal{P}_1$ or \mathcal{P}_2 depending on which TV is used. Then the optimal solution of (7) is given by $\mathbf{x}_{k+1} = \mathbf{w}_k(\mathbf{z}^*, \mathbf{P}^*, \mathbf{Q}^*)$.

Proof. Similar to [11] for the real case, the following relations for complex numbers x, y hold true

$$\begin{aligned} \sqrt{|x|^2 + |y|^2} &= \max_{p_1, p_2 \in \mathbb{C}} \{\Re(p_1^* x + p_2^* y) : |p_1|^2 + |p_2|^2 \leq 1\} \\ |x| &= \max_{p \in \mathbb{C}} \{\Re(p^* x) : |p| \leq 1\} \end{aligned}$$

where $*$ denotes the conjugate operator and $\Re(\cdot)$ represents an operator to take the real part. With these relations and the definition of TV functions, we can rewrite $\text{TV}(\mathbf{x})$ and $\|\mathbf{Tx}\|_1$ as

$$\text{TV}(\mathbf{x}) = \max_{(\mathbf{P}, \mathbf{Q}) \in \mathcal{P}} \Re \left\{ \text{vec}(\mathcal{L}(\mathbf{P}, \mathbf{Q}))^H \mathbf{x} \right\},$$

and

$$\|\mathbf{Tx}\|_1 = \max_{\mathbf{z} \in \mathcal{Z}} \Re \left\{ \mathbf{z}^H \mathbf{T} \mathbf{x} \right\}$$

where $\mathcal{P} = \mathcal{P}_1$ (respectively, \mathcal{P}_2) for TV_{iso} (respectively, TV_{ℓ_1}). Hence, we represent (7) as

$$\min_{\mathbf{x} \in \mathbb{C}^N} \max_{\substack{\mathbf{z} \in \mathcal{Z} \\ (\mathbf{P}, \mathbf{Q}) \in \mathcal{P}}} \|\mathbf{x} - \mathbf{v}_k\|_{\mathbf{B}_k}^2 + 2\bar{\lambda} g(\mathbf{x}, \mathbf{z}, \mathbf{P}, \mathbf{Q}), \quad (8)$$

where

$$g(\mathbf{x}, \mathbf{z}, \mathbf{P}, \mathbf{Q}) = \Re \left\{ \alpha \langle \mathbf{T} \mathbf{x}, \mathbf{z} \rangle + (1 - \alpha) \text{vec}(\mathcal{L}(\mathbf{P}, \mathbf{Q}))^H \mathbf{x} \right\}.$$

Reorganizing (8), we get

$$\min_{\mathbf{x} \in \mathbb{C}^N} \max_{\substack{\mathbf{z} \in \mathcal{Z} \\ (\mathbf{P}, \mathbf{Q}) \in \mathcal{P}}} \|\mathbf{x} - \mathbf{w}_k(\mathbf{z}, \mathbf{P}, \mathbf{Q})\|_{\mathbf{B}_k}^2 - \|\mathbf{w}_k(\mathbf{z}, \mathbf{P}, \mathbf{Q})\|_{\mathbf{B}_k}^2, \quad (9)$$

where

$$\mathbf{w}_k(\mathbf{z}, \mathbf{P}, \mathbf{Q}) = \mathbf{v}_k - \bar{\lambda} \mathbf{B}_k^{-1} (\alpha \mathbf{T}^H \mathbf{z} + (1 - \alpha) \text{vec}(\mathcal{L}(\mathbf{P}, \mathbf{Q}))).$$

Since (9) is convex in \mathbf{x} and concave in $(\mathbf{z}, \mathbf{P}, \mathbf{Q})$, we interchange the minimum and maximum and then get

$$\max_{\substack{\mathbf{z} \in \mathcal{Z} \\ (\mathbf{P}, \mathbf{Q}) \in \mathcal{P}}} \min_{\mathbf{x} \in \mathbb{C}^N} \|\mathbf{x} - \mathbf{w}_k(\mathbf{z}, \mathbf{P}, \mathbf{Q})\|_{\mathbf{B}_k}^2 - \|\mathbf{w}_k(\mathbf{z}, \mathbf{P}, \mathbf{Q})\|_{\mathbf{B}_k}^2. \quad (10)$$

Note that \mathbf{x} only appears in the first term of (10) so that the optimal solution of the minimum part is

$$\mathbf{x}^* = \mathbf{w}_k(\mathbf{z}, \mathbf{P}, \mathbf{Q}). \quad (11)$$

Substituting (11) into (10), we get the following dual problem that contains only unknown dual variables $(\mathbf{z}, \mathbf{P}, \mathbf{Q})$

$$(\mathbf{z}^*, \mathbf{P}^*, \mathbf{Q}^*) = \underset{\substack{\mathbf{z} \in \mathcal{Z} \\ (\mathbf{P}, \mathbf{Q}) \in \mathcal{P}}}{\text{argmin}} \|\mathbf{w}_k(\mathbf{z}, \mathbf{P}, \mathbf{Q})\|_{\mathbf{B}_k}^2. \quad (12)$$

After solving (12), the primal variable update is $\mathbf{x}_{k+1} = \mathbf{w}_k(\mathbf{z}^*, \mathbf{P}^*, \mathbf{Q}^*)$. This completes the proof. \square

With Proposition 1, we can apply the FISTA [10, 27] to solve (12) for computing $\text{prox}_{\tilde{\lambda}h}^{\mathbf{B}_k}$ since (12) is convex and continuously differentiable. Lemma 1 specifies the corresponding gradient and Lipschitz constant of (12).

Lemma 1. *The gradient of (12) is*

$$-2\tilde{\lambda} \begin{bmatrix} \alpha \mathbf{T} \\ (1-\alpha) \mathcal{L}^T \end{bmatrix} \mathbf{w}_k(\mathbf{z}, \mathbf{P}, \mathbf{Q}) \quad (13)$$

and the corresponding Lipschitz constant is

$$L_c = 2\sigma_{\min} \tilde{\lambda}^2 (\alpha^2 \|\mathbf{T}\|^2 + 8(1-\alpha)^2)$$

where σ_{\min} is the smallest eigenvalue of \mathbf{B}_k .

Proof. Denote by $h(\mathbf{z}, \mathbf{P}, \mathbf{Q}) \triangleq \|\mathbf{w}_k(\mathbf{z}, \mathbf{P}, \mathbf{Q})\|_{\mathbf{B}_k}^2$. Applying the chain rule, we can easily get

$$\nabla h(\mathbf{z}, \mathbf{P}, \mathbf{Q}) = -2\tilde{\lambda} \begin{bmatrix} \alpha \mathbf{T} \\ (1-\alpha) \mathcal{L}^T \end{bmatrix} \mathbf{w}_k(\mathbf{z}, \mathbf{P}, \mathbf{Q}).$$

Now, we compute the Lipschitz constant of $h(\mathbf{z}, \mathbf{P}, \mathbf{Q})$. For every two pairs of $(\mathbf{z}_1, \mathbf{P}_1, \mathbf{Q}_1)$ and $(\mathbf{z}_2, \mathbf{P}_2, \mathbf{Q}_2)$, we have

$$\begin{aligned} & \|\nabla h(\mathbf{z}_1, \mathbf{P}_1, \mathbf{Q}_1) - \nabla h(\mathbf{z}_2, \mathbf{P}_2, \mathbf{Q}_2)\| \\ &= 2\tilde{\lambda}^2 \left\| \begin{bmatrix} \alpha \mathbf{T} \\ (1-\alpha) \mathcal{L}^T \end{bmatrix} \mathbf{B}_k^{-1} \begin{bmatrix} \alpha \mathbf{T}^H & (1-\alpha) \mathcal{L} \\ \mathcal{L}^T & \mathbf{B}_k^{-1} \end{bmatrix} \right. \\ & \quad \left. [(\mathbf{z}_1, \mathbf{P}_1, \mathbf{Q}_1) - (\mathbf{z}_2, \mathbf{P}_2, \mathbf{Q}_2)] \right\| \\ &\leq 2\tilde{\lambda}^2 \left\| \alpha^2 \mathbf{T}^H \mathbf{T} + (1-\alpha)^2 \mathcal{L}^T \mathcal{L} \right\| \left\| \mathbf{B}_k^{-1} \right\| \\ & \quad \left\| [(\mathbf{z}_1, \mathbf{P}_1, \mathbf{Q}_1) - (\mathbf{z}_2, \mathbf{P}_2, \mathbf{Q}_2)] \right\| \\ &\leq 2\tilde{\lambda}^2 (\alpha^2 \|\mathbf{T}\|^2 + (1-\alpha)^2 \|\mathcal{L}\|^2) \sigma_{\min} \\ & \quad \left\| [(\mathbf{z}_1, \mathbf{P}_1, \mathbf{Q}_1) - (\mathbf{z}_2, \mathbf{P}_2, \mathbf{Q}_2)] \right\|, \end{aligned}$$

where σ_{\min} is the smallest eigenvalue of \mathbf{B}_k . With the proof of [11, Lemma 4.2], we know $\|\mathcal{L}\| = \sqrt{8}$ such that the Lipschitz constant of $h(\mathbf{z}, \mathbf{P}, \mathbf{Q})$ is $L_c = 2\sigma_{\min} \tilde{\lambda}^2 (\alpha^2 \|\mathbf{T}\|^2 + 8(1-\alpha)^2)$. This completes the proof. \square

According to the formulation of \mathbf{B}_k proposed in Algorithm 2, we can obtain σ_{\min} easily through¹

$$\sigma_{\min} = \begin{cases} \alpha & \text{if } \tau < 0, \\ \tau & \text{if } \langle \mathbf{m}_k - \mathbf{H}_0 \mathbf{s}_k, \mathbf{s}_k \rangle > 0, \\ \tau + \frac{\mathbf{u}^H \mathbf{u}}{\langle \mathbf{m}_k - \mathbf{H}_0 \mathbf{s}_k, \mathbf{s}_k \rangle} & \text{if } \langle \mathbf{m}_k - \mathbf{H}_0 \mathbf{s}_k, \mathbf{s}_k \rangle < 0. \end{cases}$$

The value of $\|\mathbf{T}\|$ depends on the choice of wavelets which can be computed in advance such that the computational cost of obtaining the Lipschitz constant of (12) is cheap. For completeness, we present the implementation details of FISTA for solving (12) in Algorithm 3.

Remark 1. *Compared with APMs for addressing (1), the additional cost of CQNPM is applying \mathbf{B}_k^{-1} in computing \mathbf{v}_k and \mathbf{w}_k in Algorithms 1 and 3. This inversion can be computed cheaply*

¹We note that $\langle \mathbf{m}_k - \mathbf{H}_0 \mathbf{s}_k, \mathbf{s}_k \rangle$ is real in our setting, see Observation I.

Algorithm 3 FISTA for Solving (12).

Initialization: $\mathbf{B}_k, \mathbf{v}_k, \tilde{\lambda} > 0, \alpha \in [0, 1]$, Lipschitz constant L_c , maximal iteration Max_Iter , tolerance $\epsilon > 0$, and initial values $\mathbf{z}_1, \mathbf{P}_1, \mathbf{Q}_1$.

Iteration:

```

1:  $t_1 \leftarrow 1$ .
2:  $(\bar{\mathbf{z}}_1, \bar{\mathbf{P}}_1, \bar{\mathbf{Q}}_1) \leftarrow (\mathbf{z}_1, \mathbf{P}_1, \mathbf{Q}_1)$ .
3: for  $s = 1, 2, \dots, \text{Max\_Iter}$  do
4:   Compute  $\bar{\mathbf{w}} \leftarrow \mathbf{w}_k(\bar{\mathbf{z}}_s, \bar{\mathbf{P}}_s, \bar{\mathbf{Q}}_s)$ .
5:   if  $\alpha \neq 0$  then
6:      $\mathbf{z}_{s+1} \leftarrow \text{Proj}_{\mathcal{Z}}(\bar{\mathbf{z}}_s + \frac{2\lambda\alpha}{L_c} \mathbf{T} \bar{\mathbf{w}})$ .
7:   else
8:     Set  $\mathbf{z}_{s+1}$  empty.
9:   end if
10:  if  $\alpha \neq 1$  then
11:     $(\mathbf{P}_{s+1}, \mathbf{Q}_{s+1}) \leftarrow \text{Proj}_{\mathcal{P}}((\bar{\mathbf{P}}_s, \bar{\mathbf{Q}}_s) + \frac{2\lambda(1-\alpha)}{L_c} \mathcal{L}^T \bar{\mathbf{w}})$ .
12:  else
13:    Set  $\mathbf{P}_{s+1}$  and  $\mathbf{Q}_{s+1}$  empty.
14:  end if
15:  if  $\|(\mathbf{z}_{s+1} - \mathbf{z}_s, \mathbf{P}_{s+1} - \mathbf{P}_s, \mathbf{Q}_{s+1} - \mathbf{Q}_s)\| \leq \epsilon$  then
16:    break.
17:  end if
18:   $t_{s+1} \leftarrow \frac{1 + \sqrt{1 + 4t_s^2}}{2}$ .
19:   $(\bar{\mathbf{z}}_{s+1}, \bar{\mathbf{P}}_{s+1}, \bar{\mathbf{Q}}_{s+1}) \leftarrow \begin{cases} \frac{t_{s+1} + t_s - 1}{t_{s+1}} (\mathbf{z}_{s+1}, \mathbf{P}_{s+1}, \mathbf{Q}_{s+1}) \\ - \frac{t_s - 1}{t_{s+1}} (\mathbf{z}_s, \mathbf{P}_s, \mathbf{Q}_s). \end{cases}$ .
20:   $t_s \leftarrow t_{s+1}$ .
21: end for

```

through the Woodbury matrix identity. Moreover, computing the projectors $\text{Proj}_{\mathcal{Z}}(\cdot)$ and $\text{Proj}_{\mathcal{P}}(\cdot)$ is also cheap and identical to the one shown in [11], so we omit the details here. The step-size a_k in Algorithm 1 can be simply set to be 1. The parameter γ in Algorithm 2 scales the initial Hessian matrix \mathbf{H}_0 to guarantee that \mathbf{B}_k is Hermitian positive definite. In our numerical experiments, we found that a fixed γ works well in practice.

For $\alpha = 1$, running Algorithm 3 to compute the WPM is inefficient since we would have to apply wavelet transform many times at each outer iteration. However, if \mathbf{T} is invertible, we can solve the following problem instead of (1) to avoid using Algorithm 3 to compute the WPM:

$$\bar{\mathbf{x}}^* = \underset{\bar{\mathbf{x}} \in \mathbb{C}^{\tilde{N}}}{\text{argmin}} \underbrace{\frac{1}{2} \|\mathbf{A} \mathbf{T}^{-1} \bar{\mathbf{x}} - \mathbf{y}\|_2^2}_{f(\bar{\mathbf{x}})} + \lambda \|\bar{\mathbf{x}}\|_1. \quad (14)$$

Then the recovered image is $\mathbf{x}^* = \mathbf{T}^{-1} \bar{\mathbf{x}}^*$. Now the corresponding WPM becomes

$$\text{prox}_{\tilde{\lambda} \|\cdot\|_1}^{\mathbf{B}_k}(\mathbf{v}_k) = \underset{\bar{\mathbf{x}} \in \mathbb{C}^{\tilde{N}}}{\text{argmin}} \|\bar{\mathbf{x}} - \mathbf{v}_k\|_{\mathbf{B}_k}^2 + 2\tilde{\lambda} \|\bar{\mathbf{x}}\|_1. \quad (15)$$

Let $\mathbf{W} \in \mathbb{C}^{\tilde{N} \times \tilde{N}} := \mathbf{D} \pm \mathbf{u} \mathbf{u}^H$ where $\mathbf{D} \in \mathbb{R}^{\tilde{N} \times \tilde{N}}$ is a diagonal matrix and $\mathbf{u} \in \mathbb{C}^{\tilde{N}}$. Becker et al. proposed the following theorem that relates $\text{prox}_{\lambda h}^{\mathbf{B}_k}(\mathbf{x})$ and $\text{prox}_{\lambda h}^{\mathbf{D}}(\mathbf{x})$.

Theorem 1 (Theorem 3.4, [22]²). Let $\mathbf{W} = \mathbf{D} \pm \mathbf{u}\mathbf{u}^H$. Then,

$$\text{prox}_{\lambda h}^{\mathbf{W}}(\mathbf{x}) = \text{prox}_{\lambda h}^{\mathbf{D}}(\mathbf{x} \mp \mathbf{D}^{-1}\mathbf{u}\beta^*),$$

where $\beta^* \in \mathbb{C}$ is the unique zero of the following nonlinear equation

$$\mathbb{J}(\beta) : \mathbf{u}^H \left(\mathbf{x} - \text{prox}_{\lambda h}^{\mathbf{D}}(\mathbf{x} \mp \mathbf{D}^{-1}\mathbf{u}\beta) \right) + \beta.$$

From Algorithm 2, we have $\mathbf{m}_k = \mathbf{A}^H \mathbf{A} \mathbf{s}_k$, leading to the following observation:

Observation I. τ and $\langle \mathbf{m}_k - \mathbf{H}_0 \mathbf{s}_k, \mathbf{s}_k \rangle$ in Algorithm 2 are real.

Since $\langle \mathbf{m}_k - \mathbf{H}_0 \mathbf{s}_k, \mathbf{s}_k \rangle$ is real, we can rewrite \mathbf{B}_k as

$$\mathbf{B}_k = \mathbf{H}_0 + \text{sgn}(\langle \mathbf{m}_k - \mathbf{H}_0 \mathbf{s}_k, \mathbf{s}_k \rangle) \tilde{\mathbf{u}}_k \tilde{\mathbf{u}}_k^H, \quad (16)$$

where $\tilde{\mathbf{u}}_k = \frac{\mathbf{u}_k}{\sqrt{\langle \mathbf{m}_k - \mathbf{H}_0 \mathbf{s}_k, \mathbf{s}_k \rangle}}$ and $\text{sgn}(\cdot)$ denotes the sign function such that \mathbf{B}_k holds the same structure as \mathbf{W} in Theorem 1. So, instead of solving (15) directly, we address $\mathbb{J}(\beta) = 0$ first and then use Theorem 1 to obtain $\text{prox}_{\frac{\lambda}{\|\cdot\|_1}}^{\mathbf{B}_k}(\mathbf{v}_k)$. In this paper, we solve $\mathbb{J}(\beta) = 0$ using “SciPy” library in Python.

For $\alpha \in (0, 1)$, Algorithm 3 still requires applying wavelet transforms many times, which can dominate the computational cost. An alternative way is to use the idea proposed in [28] where one partially smooths the objective and then applies Algorithm 1. For comparison purposes, we apply Algorithm 1 to the following problem

$$\min_{\mathbf{x} \in \mathbb{C}^N} \underbrace{\frac{1}{2} \|\mathbf{Ax} - \mathbf{y}\|_2^2 + \lambda \alpha \cdot S^\eta(\|\mathbf{Tx}\|_1)}_{f(\mathbf{x})} + \underbrace{\lambda(1 - \alpha) \text{TV}(\mathbf{x})}_{h(\mathbf{x})}, \quad (17)$$

such that each outer iteration needs only two wavelet transforms. For the comparisons in this paper, we used $S^\eta(\|\mathbf{x}\|_1) = \sum_{n=1}^N \sqrt{x_n^2 + \eta}$ with $\eta > 0$ so that $f(\mathbf{x})$ in (17) is differentiable. Our numerical experiments compare the performance of such a partial smoothing approach to methods based on the original cost function for image reconstruction in CS MRI.³

IV. NUMERICAL EXPERIMENTS

This section studies the performance of our algorithm for image reconstruction in CS MRI with spiral and radial trajectories. Similar to [1], we mainly consider wavelet and TV regularizers. We took complex k-space data from the brain and knee training datasets (one each) in the NYU fastMRI dataset [29] to generate the simulated k-space data. We applied the ESPIRiT algorithm [30] to recover the complex images and then cropped the images to size 256×256 to define the ground-truth images, with maximum magnitude scaled to one. Figure 1 shows the magnitude of the complex-valued ground-truth images. Following [13], we used 32 interleaves, 1688 readout points, and 12-coils (respectively, 96 radial projections, 512 readout points, and 12 coils) for the spiral (respectively, radial) trajectory to define the forward model \mathbf{A} . Applying the used forward model to the ground truth image generated

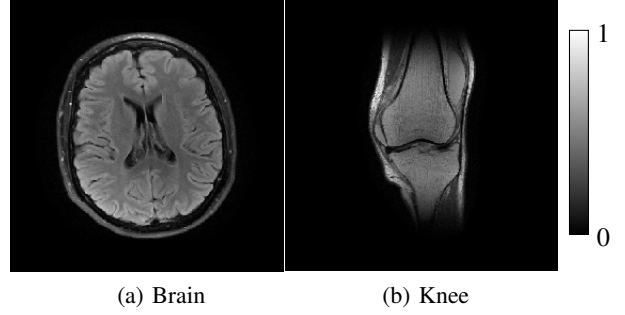


Fig. 1. The magnitude of the complex-valued ground truth images.

the noiseless multi-coil k-space data. We added complex i.i.d Gaussian noise with mean zero and variance 10^{-2} to all coils to form the measurements, \mathbf{y} . Our implementation used Python programming language with SigPy library [31]. The reconstructions ran on a workstation with 2.3GHz AMD EPYC 7402. Our code will be released after paper acceptance.

Algorithm Settings: For APM, we precomputed the Lipschitz constant for all experiments. For CQNPM, we set $a_k = 1$ and $\gamma = 1.7$. Denote by S-APM (respectively, S-CQNPM) when APM (respectively, CQNPM) is used to solve (17). We chose the step-size in S-APM using a backtracking strategy [32]. The trade-off parameters λ and α were chosen to reach the highest peak signal-to-noise ratio (PSNR) when running enough iterations of APM. We set $\eta = 10^{-4}$ in our experiments.

A. Radial Acquisition MRI Reconstruction

Figure 2 shows the performance of Algorithm 1 for the wavelet based reconstruction of the brain image and the comparison with APM [10]. Clearly CQNPM converged faster than APM in terms of the number of iterations. Compared with the cost of computing the proximal mapping, the additional cost of computing WPM with our method is insignificant. Indeed, Figure 2 shows that CQNPM also needed less CPU time to reach a lower cost than APM. The comparison of PSNR versus CPU time also shows that CQNPM reached a higher PSNR with less CPU time, illustrating the fast convergence of CQNPM. The reconstructed images at 3, 10, and 16th iteration illustrate that CQNPM yielded a clearer image than APM for the same number of iterations. Similar observations apply to the knee image; see Figure 3.

We also studied the performance of our algorithm when using both wavelet and TV regularizers. Since ADMM is a classical method for (2) with $h(\mathbf{x}) = \alpha \|\mathbf{Tx}\|_1 + (1 - \alpha) \text{TV}(\mathbf{x})$, we include a comparison with ADMM. Moreover, we also studied the performance of the partially smoothing technique. Figure 4 presents the results for the reconstruction of the brain image. Although we solved (17) instead of (2) for the partially smoothing method, the cost is still computed with (2). Surprisingly, we see that, for the cost value versus iterations, S-APM (respectively, S-CQNPM) converged similar to APM (respectively, CQNPM). However, from the cost value versus CPU time plot, we observe that S-APM (respectively, S-CQNPM) converged faster than APM (respectively, CQNPM)

²The theorem is proved in real plane but it is also valid in complex plane.

³One could instead partially smooth the TV regularizer. However, in our settings, we found that smoothing $\|\mathbf{Tx}\|_1$ led to better quality than TV smoothing.

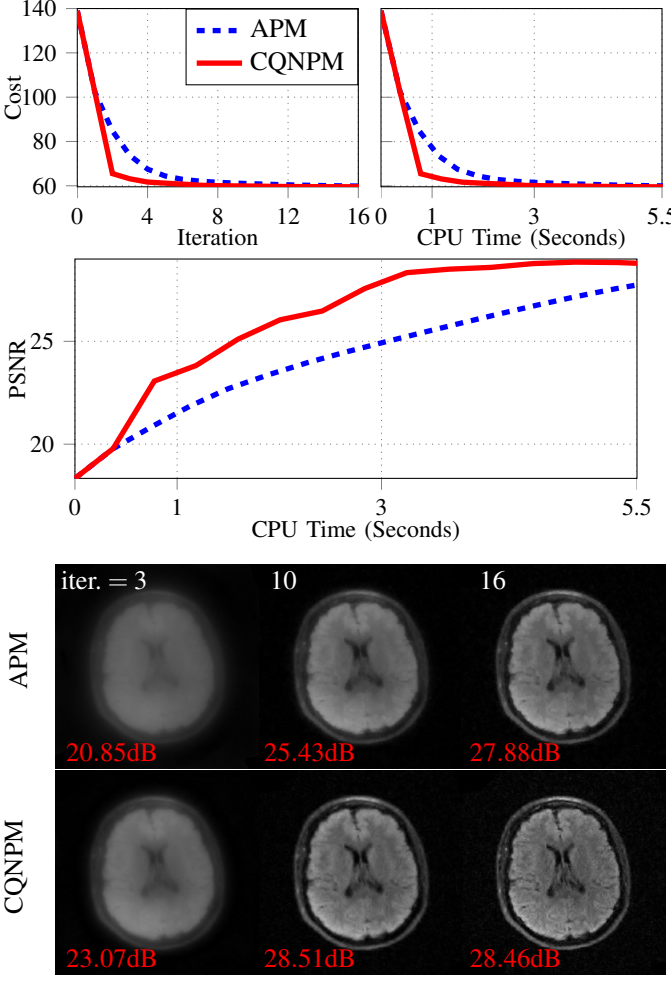


Fig. 2. Performance of the brain image with regularizer $h(\mathbf{x}) = \|\mathbf{T}\mathbf{x}\|_1$ and $\lambda = 5 \times 10^{-4}$ for an orthonormal wavelet transform \mathbf{T} with 5 levels. Acquisition: radial trajectory with 96 projections, 512 readout points, and 12 coils.

in terms of CPU time, as expected since the partially smoothing method requires only two wavelet transforms per outer iteration. The PSNR versus CPU time plot also demonstrates the fast convergence of CQNPM and S-CQNPM. The reconstructed images at 3, 10, and 16th iteration for each method⁴ illustrate that the partial smoothing method works as well as the nonsmoothing one. In summary, the proposed method converged faster than other methods in terms of the number of iterations and CPU time, and S-CQNPM is the best algorithm for (2) in this setting. Similar observations apply to the knee image; see Figure 5.

B. Spiral Acquisition MRI Reconstruction

This part studies the reconstruction with spiral acquisition that used 32 interleaves, 1688 readout points, and 12 coils. Figures 6 to 9 show the results of the brain and knee images with wavelet and TV regularizers. The trends are similar to the radial acquisition case.

⁴We do not show the reconstructed image of ADMM since it yielded a much lower PSNR than other methods.

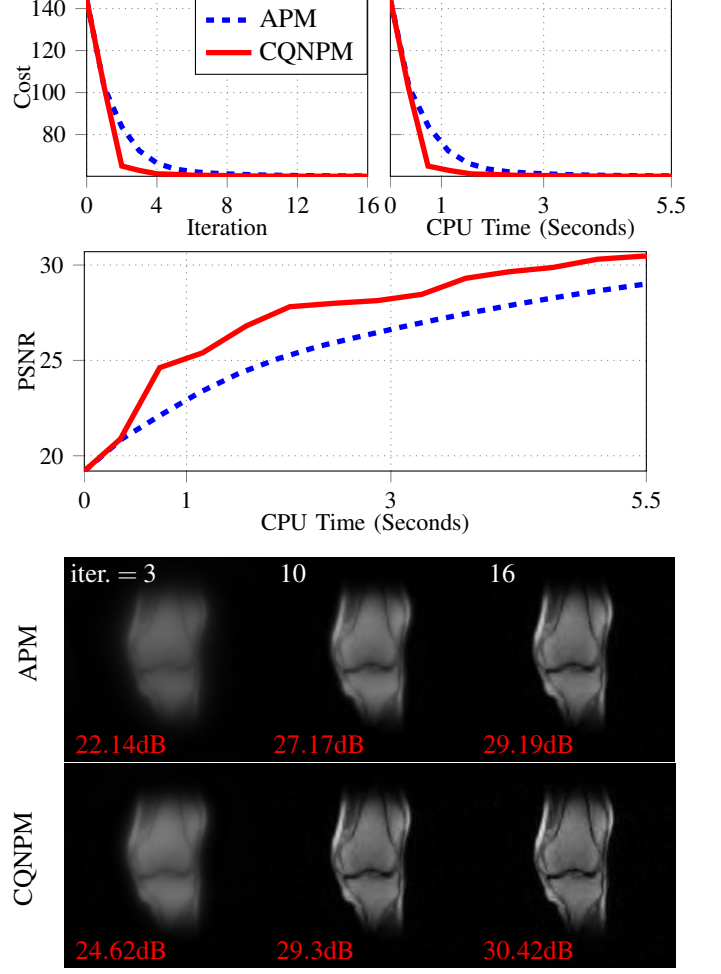


Fig. 3. Performance of the knee image with same regularizer and acquisition as Figure 2. The parameter λ was 10^{-3} .

C. The Choice of γ

We tried several different γ values to study how γ affects the convergence of CQNPM. We reconstructed the brain image with wavelet and TV regularizers and spiral acquisition. Figure 10 presents the results that show that CQNPM is quite robust to different γ values, and $\gamma = 1.7$ worked slightly better than the others. So we simply set $\gamma = 1.7$ for all experiments.

V. CONCLUSIONS AND FUTURE WORK

This paper proposes complex quasi-Newton proximal methods for solving (2) that led to faster convergence than APMs. By using the structure of \mathbf{B}_k , we develop efficient approaches for computing the WPM. Compared with computing the proximal mapping in APMs, i.e., $\mathbf{B}_k = \mathbf{I}_N$, the increased computational cost in computing the WPM is insignificant, as illustrated by our comparisons in terms of CPU time. CQNPM is appealing for large-scale problems because CQNPM requires fewer iterations than APMs to converge, reducing the times of computing $\nabla f(\mathbf{x})$ that it is expensive in large-scale settings. Interestingly, in our setting, we found the partial smoothing method worked pretty well when both wavelet and TV regularizers are used. So the partial smoothing approach

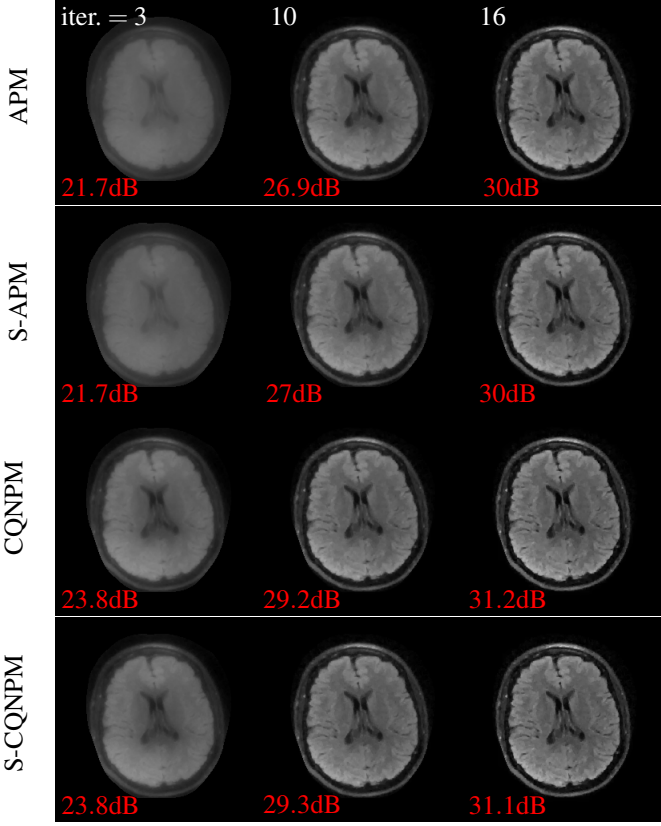
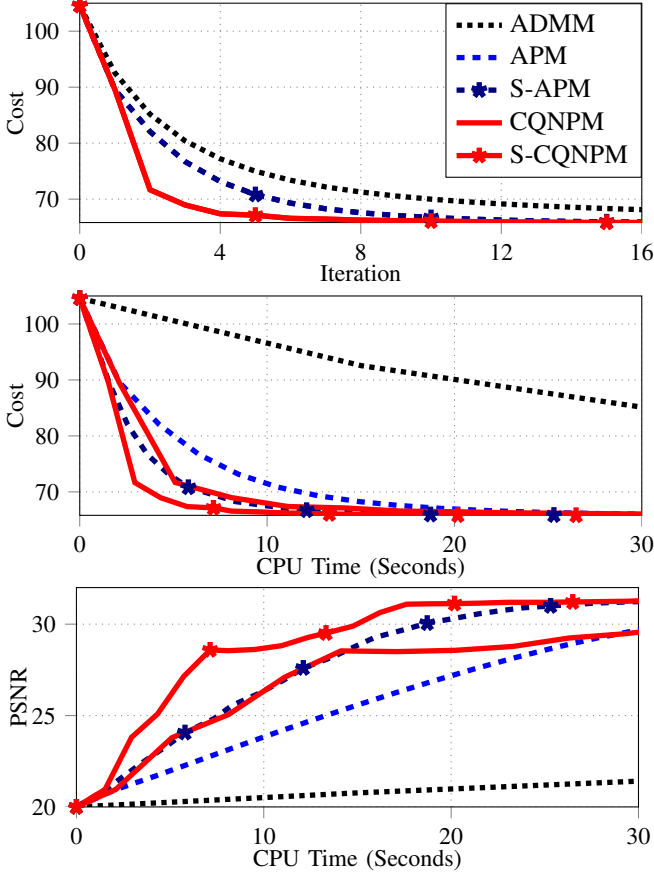


Fig. 4. Performance of the brain image with regularizer $h(\mathbf{x}) = \alpha \|\mathbf{Tx}\|_1 + (1 - \alpha)TV(\mathbf{x})$ and same acquisition as Figure 2. The parameters were $\lambda = 6 \times 10^{-4}$ and $\alpha = \frac{1}{6}$.

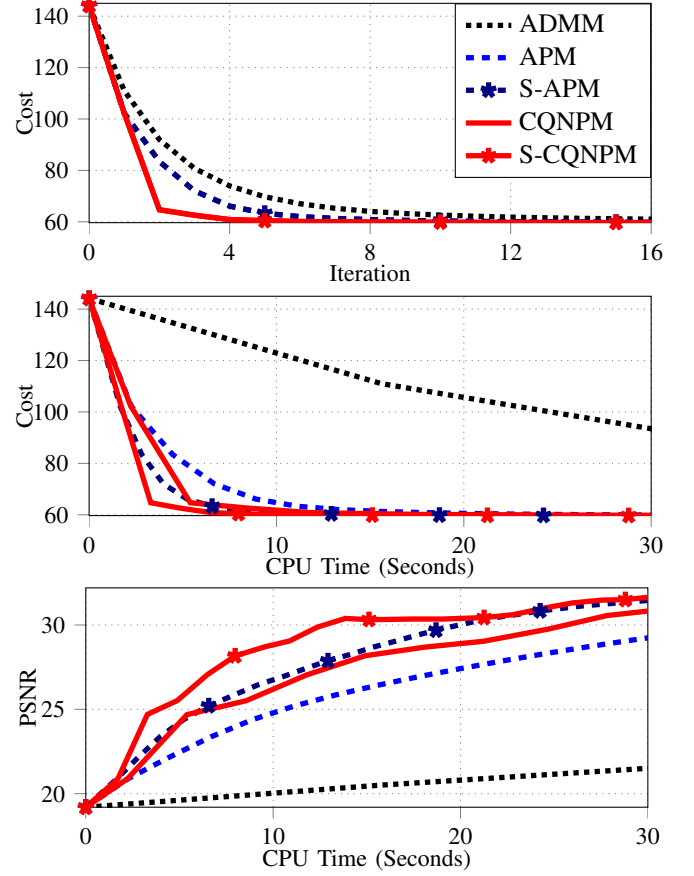


Fig. 5. Performance of the knee image with same regularizer and acquisition as Figure 2. The parameters λ and α were 10^{-3} and $\frac{1}{2}$.

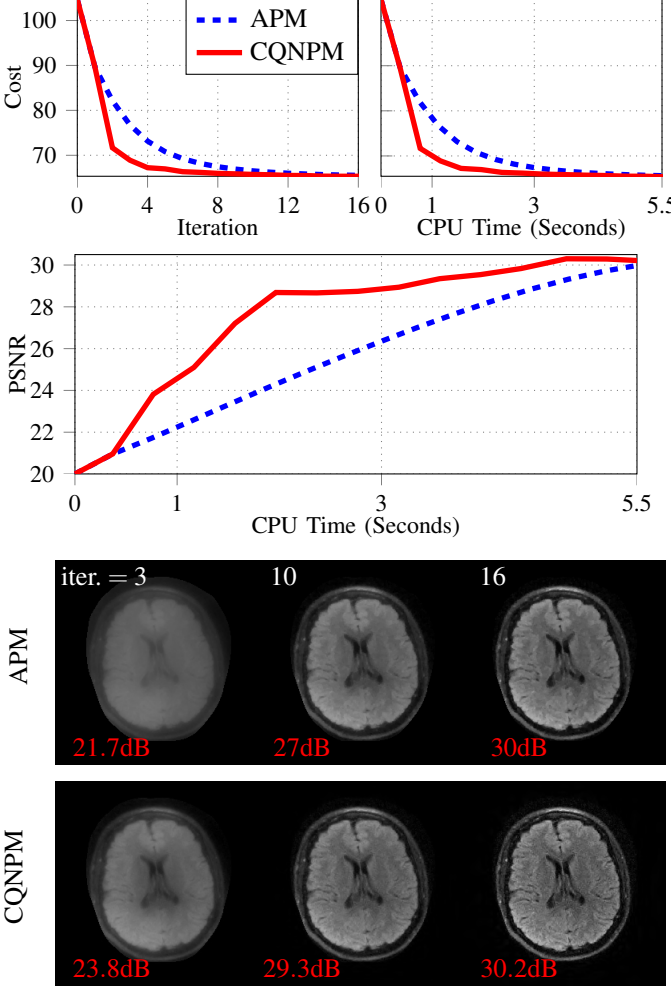


Fig. 6. Performance of the brain image with regularizer $h(\mathbf{x}) = \|\mathbf{T}\mathbf{x}\|_1$ and $\lambda = 10^{-3}$ for an orthonormal wavelet transform \mathbf{T} with 5 levels. Acquisition: spiral trajectory with 32 intervals, 1688 readout points, and 12 coils.

may be a good method for solving problems with two nonsmooth terms. However, a backtracking line search is needed that may increase the computation for different applications.

Clearly, \mathbf{B}_k plays an important role in our algorithm and a more accurate \mathbf{B}_k can accelerate the convergence further. Since the Hessian matrix in CS MRI is known, i.e., $\mathbf{A}^H \mathbf{A}$, we plan to learn a fixed weighting \mathbf{B} to approximate $\mathbf{A}^H \mathbf{A}$ accurately for future work. However, \mathbf{B} must be easy to invert so that \mathbf{B} should have some special structures, e.g., $\mathbf{B} = \mathbf{D} \pm \mathbf{U} \mathbf{U}^H$. Moreover, with such a fixed \mathbf{B} , we can adopt the accelerated manner used in APMs for Algorithm 1 and obtain an even faster algorithm than the one presented here.

VI. ACKNOWLEDGEMENTS

This work was funded by National Institutes of Health grant R01NS112233.

REFERENCES

[1] M. Lustig, D. Donoho, and J. M. Pauly, “Sparse MRI: The application of compressed sensing for rapid MR

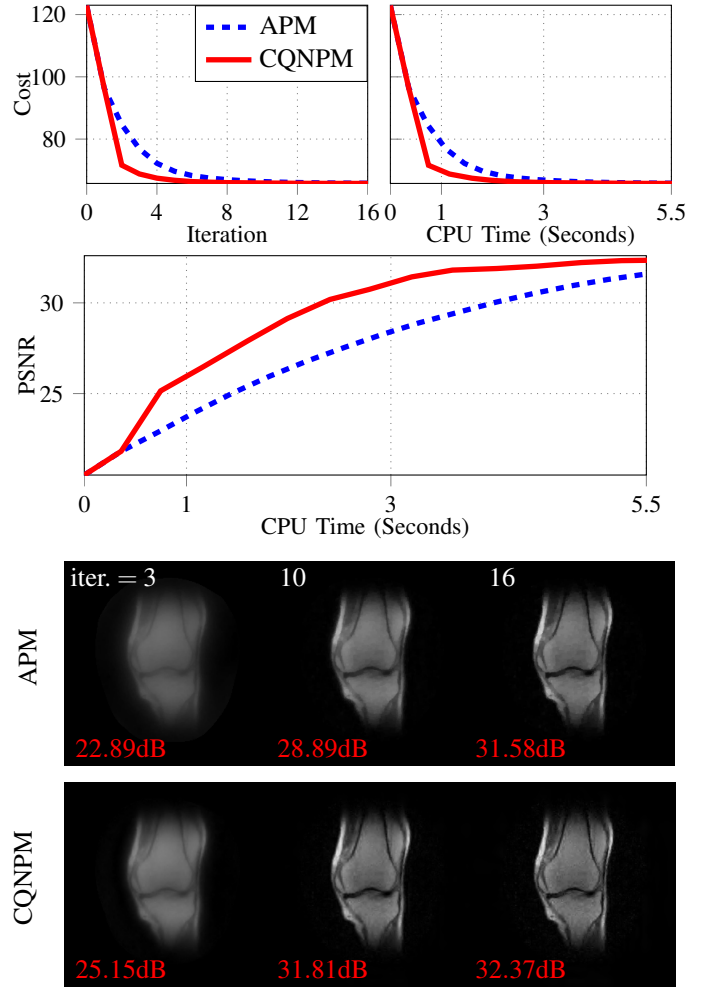


Fig. 7. Performance of the knee image with same regularizer and acquisition as Figure 6. The parameter λ was 2×10^{-3} .

imaging,” *Magnetic Resonance in Medicine*, vol. 58, no. 6, pp. 1182–1195, 2007.

[2] M. Guerquin-Kern, M. Haberlin, K. P. Pruessmann, and M. Unser, “A fast wavelet-based reconstruction method for magnetic resonance imaging,” *IEEE Transactions on Medical Imaging*, vol. 30, no. 9, pp. 1649–1660, 2011.

[3] S. Ravishankar and Y. Bresler, “MR image reconstruction from highly undersampled k-space data by dictionary learning,” *IEEE Transactions on Medical Imaging*, vol. 30, no. 5, pp. 1028–1041, 2011.

[4] W. Dong, G. Shi, X. Li, Y. Ma, and F. Huang, “Compressive sensing via nonlocal low-rank regularization,” *IEEE Transactions on Image Processing*, vol. 23, no. 8, pp. 3618–3632, 2014.

[5] S. V. Venkatakrishnan, C. A. Bouman, and B. Wohlberg, “Plug-and-play priors for model based reconstruction,” in *IEEE Global Conference on Signal and Information Processing*. IEEE, 2013, pp. 945–948.

[6] R. Ahmad, C. A. Bouman, G. T. Buzzard, S. Chan, S. Liu, E. T. Reehorst, and P. Schniter, “Plug-and-play methods for magnetic resonance imaging: Using denoisers for image recovery,” *IEEE Signal Processing*

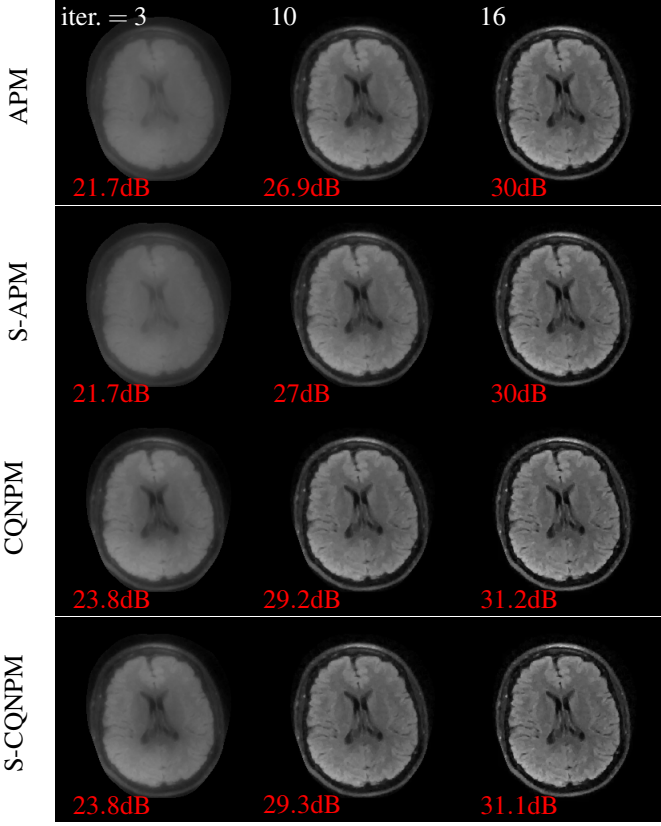
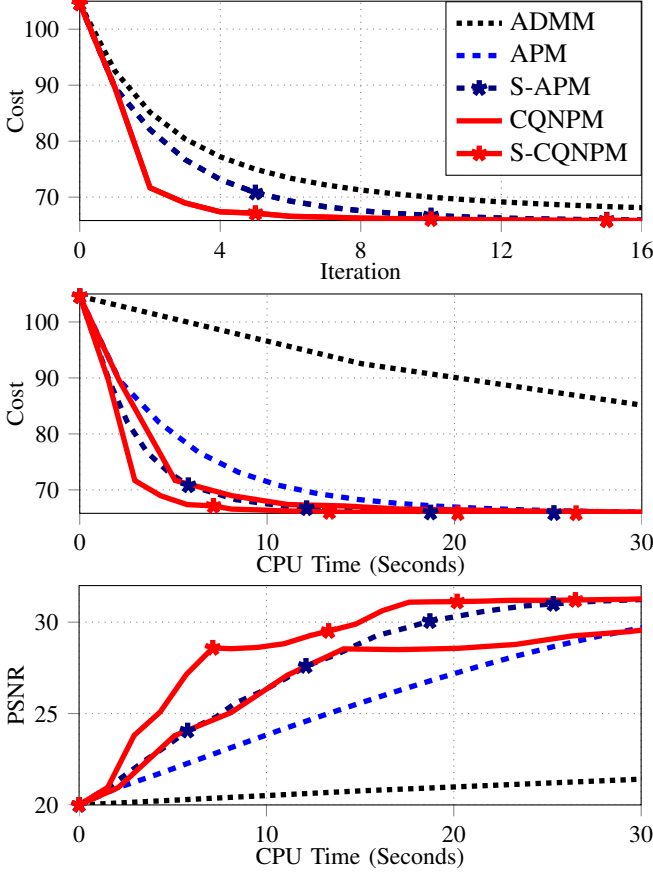


Fig. 8. Performance of the brain image with regularizer $h(\mathbf{x}) = \alpha \|\mathbf{T}\mathbf{x}\|_1 + (1-\alpha)TV(\mathbf{x})$ and same acquisition as Figure 6. The parameters λ and α were 10^{-3} and $\frac{1}{2}$.

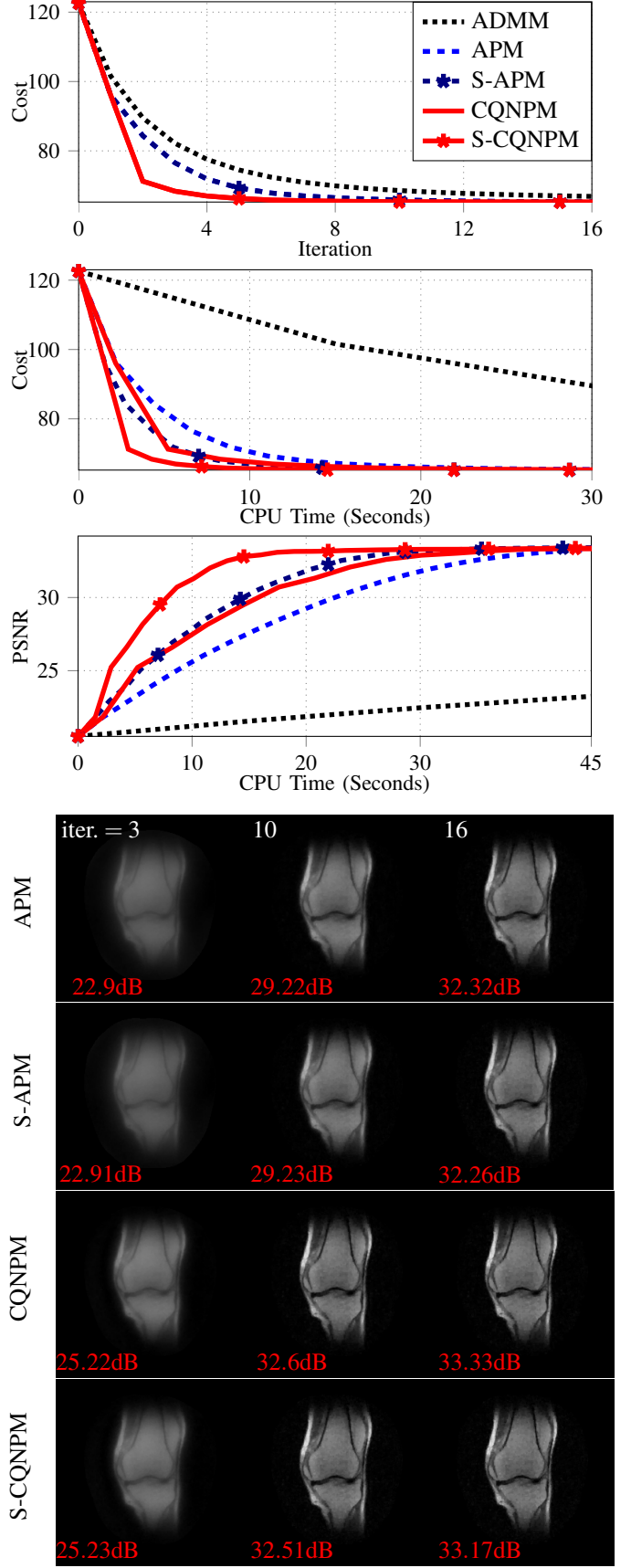


Fig. 9. Performance of the knee image with same regularizer and acquisition as Figure 6. The parameters λ and α were 10^{-3} and $\frac{1}{2}$.

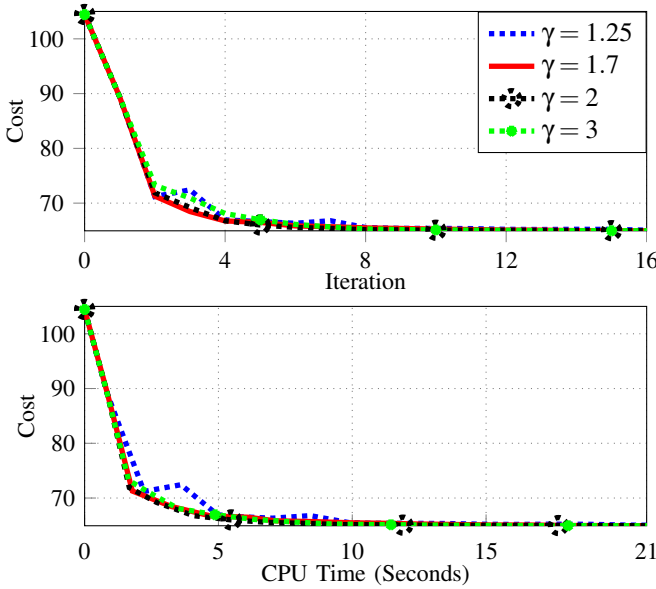


Fig. 10. The influence of γ on the convergence of CQNPM. Test on the brain image with the wavelet and TV regularizers and spiral acquisition.

Magazine, vol. 37, no. 1, pp. 105–116, 2020.

- [7] H. K. Aggarwal, M. P. Mani, and M. Jacob, “MoDL: Model-based deep learning architecture for inverse problems,” *IEEE Transactions on Medical Imaging*, vol. 38, no. 2, pp. 394–405, 2018.
- [8] Y. Song, L. Shen, L. Xing, and S. Ermon, “Solving inverse problems in medical imaging with score-based generative models,” in *International Conference on Learning Representations*, 2021.
- [9] N. Parikh, S. Boyd *et al.*, “Proximal algorithms,” *Foundations and Trends® in Optimization*, vol. 1, no. 3, pp. 127–239, 2014.
- [10] A. Beck and M. Teboulle, “A fast iterative shrinkage-thresholding algorithm for linear inverse problems,” *SIAM Journal on Imaging Sciences*, vol. 2, no. 1, pp. 183–202, 2009.
- [11] ———, “Fast gradient-based algorithms for constrained total variation image denoising and deblurring problems,” *IEEE Transactions on Image Processing*, vol. 18, no. 11, pp. 2419–2434, 2009.
- [12] J. A. Fessler, “Optimization methods for magnetic resonance image reconstruction: Key models and optimization algorithms,” *IEEE Signal Processing Magazine*, vol. 37, no. 1, pp. 33–40, 2020.
- [13] S. S. Iyer, F. Ong, X. Cao, C. Liao, D. Luca, J. I. Tamir, and K. Setsompop, “Polynomial preconditioners for regularized linear inverse problems,” *arXiv preprint arXiv:2204.10252*, 2022.
- [14] F. Ong, M. Uecker, and M. Lustig, “Accelerating non-cartesian MRI reconstruction convergence using k-space preconditioning,” *IEEE Transactions on Medical Imaging*, vol. 39, no. 5, pp. 1646–1654, 2019.
- [15] S. Boyd, N. Parikh, E. Chu, B. Peleato, J. Eckstein *et al.*, “Distributed optimization and statistical learning via the alternating direction method of multipliers,” *Foundations and Trends® in Machine Learning*, vol. 3, no. 1, pp. 1–122, 2011.
- [16] B. He and X. Yuan, “On the $O(1/n)$ convergence rate of the douglas–rachford alternating direction method,” *SIAM Journal on Numerical Analysis*, vol. 50, no. 2, pp. 700–709, 2012.
- [17] S. Ramani and J. A. Fessler, “Parallel MR image reconstruction using augmented lagrangian methods,” *IEEE Transactions on Medical Imaging*, vol. 30, no. 3, pp. 694–706, 2010.
- [18] D. S. Weller, S. Ramani, and J. A. Fessler, “Augmented lagrangian with variable splitting for faster non-cartesian ℓ_1 -SPIRiT MR image reconstruction,” *IEEE Transactions on Medical Imaging*, vol. 33, no. 2, pp. 351–361, 2013.
- [19] K. Koolstra, J. van Gemert, P. Börnert, A. Webb, and R. Remis, “Accelerating compressed sensing in parallel imaging reconstructions using an efficient circulant preconditioner for cartesian trajectories,” *Magnetic Resonance in Medicine*, vol. 81, no. 1, pp. 670–685, 2019.
- [20] J. Nocedal and S. J. Wright, *Numerical Optimization*. Springer, 2006.
- [21] J. D. Lee, Y. Sun, and M. A. Saunders, “Proximal Newton-type methods for minimizing composite functions,” *SIAM Journal on Optimization*, vol. 24, no. 3, pp. 1420–1443, 2014.
- [22] S. Becker, J. Fadili, and P. Ochs, “On quasi-Newton forward-backward splitting: Proximal calculus and convergence,” *SIAM Journal on Optimization*, vol. 29, no. 4, pp. 2445–2481, 2019.
- [23] T. Hong, I. Yavneh, and M. Zibulevsky, “Solving RED with weighted proximal methods,” *IEEE Signal Processing Letters*, vol. 27, pp. 501–505, 2020.
- [24] A. Kadu, H. Mansour, and P. T. Boufounos, “High-contrast reflection tomography with total-variation constraints,” *IEEE Transactions on Computational Imaging*, vol. 6, pp. 1523–1536, 2020.
- [25] T. Ge, U. Villa, U. S. Kamilov, and J. A. O’Sullivan, “Proximal Newton methods for X-ray imaging with non-smooth regularization,” *Electronic Imaging*, vol. 2020, no. 14, pp. 7–1, 2020.
- [26] A. Chambolle, “An algorithm for total variation minimization and applications,” *Journal of Mathematical Imaging and Vision*, vol. 20, no. 1, pp. 89–97, 2004.
- [27] Y. Nesterov, “A method for unconstrained convex minimization problem with the rate of convergence $O(1/k^2)$,” in *Doklady an SSSR*, vol. 269, no. 3, 1983, pp. 543–547.
- [28] A. Beck and M. Teboulle, “Smoothing and first order methods: A unified framework,” *SIAM Journal on Optimization*, vol. 22, no. 2, pp. 557–580, 2012.
- [29] J. Zbontar, F. Knoll, A. Sriram, T. Murrell, Z. Huang, M. J. Muckley, A. Defazio, R. Stern, P. Johnson, M. Bruno *et al.*, “fastMRI: An open dataset and benchmarks for accelerated MRI,” *arXiv preprint arXiv:1811.08839*, 2018.
- [30] M. Uecker, P. Lai, M. J. Murphy, P. Virtue, M. Elad, J. M. Pauly, S. S. Vasanawala, and M. Lustig, “ESPIRiT—an eigenvalue approach to autocalibrating parallel MRI: where SENSE meets GRAPPA,” *Magnetic Resonance in*

Medicine, vol. 71, no. 3, pp. 990–1001, 2014.

[31] F. Ong and M. Lustig, “SigPy: a python package for high performance iterative reconstruction,” in *Proceedings of the ISMRM 27th Annual Meeting, Montreal, Quebec, Canada*, vol. 4819, 2019.

[32] A. Beck, *First-Order Methods in Optimization*. SIAM, 2017, vol. 25.